

Diffraction at HERA

BERND LÖHR

DESY

1. Diffraction High Energy Particle Scattering

In high-energy particle scattering, interactions are mediated by the exchange of particles between the scattering partners. Regge theory [1], and in a wider sense Regge phenomenology [2], provides a framework for the successful description of many peripheral high-energy hadronic reactions. Conceptionally the most simple peripheral diffractive process is elastic scattering. In Regge theory a new, hypothetical object, the pomeron(IP) [3], has been introduced as the exchanged object to describe elastic scattering, in particular the rise of the cross section with center-of-mass-energy. The pomeron carries the quantum numbers of the vacuum with the exception of spin. If the pomeron transfers enough energy one partner or both may dissociate into a multi-particle state giving rise to inelastic diffractive reactions. The possible reactions are visualised in Fig.1.

2. Kinematics of Deep Inelastic Scattering and Diffractive Deep Inelastic Scattering

In deep-inelastic electron-proton scattering (DIS) at the HERA collider [4], we are dealing with the process which is sketched in Fig.2. The word electron is further used generically for electrons and positrons. The incoming electron emits a virtual photon which interacts with one of the quarks in the proton. The struck quark receives a transverse momentum and separates from the remnant of the proton. A colour string stretches between them. Finally, the colour string breaks up and the system of the proton remnant, the struck quark, and the colour string fragments into hadrons which fill the region between the initial proton direction and the struck quark direction. The kinematics of inclusive DIS is described by the following variables:

$$\begin{aligned}
s &= (k+p)^2 && : \text{center-of-mass-energy squared of the e-p system,} \\
Q^2 &= -q^2 = -(k-k')^2 && : \text{negative momentum transfer squared at the} \\
&&& \text{electron vertex,} \\
W^2 &= M_h^2 = (p+q)^2 && : \text{cms energy of the virtual photon and the proton,} \\
&&& \text{mass of the hadronic system in the final state,} \\
x &= \frac{Q^2}{2p \cdot q} && : \text{the fraction of the proton momentum carried} \\
&&& \text{by the struck quark,} \\
y &= \frac{p \cdot q}{p \cdot k} && : \text{fraction of the electron momentum transferred to} \\
&&& \text{the proton in its rest system.}
\end{aligned}$$

These variables are not all independent. They are connected by the relation $Q^2 = x \cdot y \cdot s$.

In diffractive scattering, the virtual photon interacts with a pomeron, as shown in Fig. 3. The proton remains intact or dissociates into a low-mass hadronic system N. The virtual photon and the pomeron form a hadronic system X. Because the systems X and p(N) are not connected by a coloured string the hadronic system X is well separated from the proton. This leads to a gap in (pseudo)rapidity, $\eta = -\ln \tan(\Theta/2)$, between the proton(N) and the system X. Here Θ is the angle between the proton direction, called forward, and the first detected particle from the system X. Additional variables are needed to describe diffractive scattering:

$$\begin{aligned}
M_X &&& : \text{mass of the diffractively produced} \\
&&& \text{hadronic system X,} \\
t &= (p-p')^2 && : \text{four momentum transfer squared at} \\
&&& \text{the proton vertex,} \\
x_{\mathcal{P}} &= \frac{(p-p') \cdot q}{p \cdot q} = \frac{M_X^2 + Q^2}{W^2 + Q^2} && : \text{fraction of the proton momentum} \\
&&& \text{carried by the exchanged pomeron,} \\
\beta &= \frac{Q^2}{2(p-p') \cdot q} = \frac{Q^2}{M_X^2 + Q^2} = \frac{x}{x_{\mathcal{P}}} && : \text{momentum fraction of the pomeron} \\
&&& \text{that is involved in the hard scattering.}
\end{aligned}$$

3. Regge phenomenology versus perturbative QCD

Hadronic reactions in peripheral processes have been studied extensively and can be described in the framework of Regge phenomenology. In Regge theory, the exchanged object between the target proton and the incoming projectile is a Regge trajectory, also called a reggeon. A Regge trajectory describes the exchange of a system of generalized particles with continuous spin but otherwise the same quantum numbers. Trajectories are parametrised to be linear

$$\alpha_R(t) = \alpha_R(0) + \alpha' \cdot t .$$

All the trajectories, on which known particles lie, have an intercept $\alpha_R(0)$ smaller than one. This has the consequence that their contribution to the total cross-section falls with energy. It is an experimental fact that at high energies the total hadronic cross-sections rise with energy because they include the elastic process described by pomeron exchange. At high enough energies, this pomeron contribution will dominate. Diffractive reactions are mediated by the pomeron trajectory. Their cross sections are given by:

$$\frac{d\sigma}{dt} \propto e^{b(W) \cdot t} \left(\frac{W}{W_0} \right)^{4(\alpha_P(t)-1)} \quad \sigma_{tot} \propto \left(\frac{W}{W_0} \right)^{2(\alpha_P(0)-1)}$$

$$\text{with } b(W) = b_0 + 4\alpha' \cdot \ln \left(\frac{W}{W_0} \right) .$$

In DIS, W is the center-of-mass-energy of the virtual photon plus the proton. From the analyses of many peripheral hadronic processes the pomeron trajectory was found to be [5]:

$$\alpha_P(t) = 1.08 + 0.25 \cdot t .$$

The predictions from Regge theory for soft diffractive processes are a power-law behavior of the total diffractive γ^* -p cross-section as $\sigma(W) \propto W^\delta$ with and an exponential drop of the differential cross section as a function of t , (note: t is negative), with an increasing slope, $b(W)$, as W increases. This last fact is called shrinkage.

Diffractive deep-inelastic scattering at high photon-virtualities, Q^2 , (hard diffraction) is expected to be described by perturbative QCD because high Q^2 provides a hard scale. This can be conveniently formulated in terms of the colour-dipole picture. The virtual photon splits into a quark-antiquark pair at an early time before the interaction and the quark-antiquark pair interacts with the proton as shown in Fig.4. In the simplest approach the interaction takes place by the exchange of two gluons which form a colour singlet. In the next order, the quark-antiquark pair radiates a gluon to

which one of the exchanged gluons couples. This is sketched in Fig.5. In higher orders of pQCD, the exchanged gluon system is commonly treated as a BFKL-type ladder [6]. In the colour-dipole picture, the transverse separation of the q and the \bar{q} , r , is given by the virtuality Q^2 , the quark mass m_q , and the momentum fractions z and $(1 - z)$ of the quark and antiquark, respectively:

$$r \propto \frac{1}{z(1 - z)Q^2 + m_q^2}.$$

Various pQCD inspired models exist for the hard diffractive-scattering. All these models predict little or no shrinkage.

4. Exclusive vector-meson production

Exclusive vector-meson production is a diffractive process and has been studied extensively. The vector-meson dominance model (VMD) [7] plus Regge theory provide a framework in which exclusive vector-meson production is understood as a quasi-elastic scattering where the incoming vector meson is off mass shell. The situation is graphically shown in Fig.6. In pQCD, exclusive vector-meson production in the colour-dipole picture proceeds according to Fig.7. Perturbative QCD is expected to be applicable when the transverse dimension, r , of the quark-antiquark system gets small. This happens when either Q^2 or m_q get big. Perturbative QCD models predict a rise of the cross section like $\sigma(W) \propto W^\delta$ with $\delta \approx 0.8$ which is faster than expected from Regge theory. The slope of the t distribution is predicted to be $b \approx 4$ GeV and $\alpha' \approx 0$. This means no or little shrinkage. The conditions under which exclusive vector-meson production is a hard diffractive process that can be described by pQCD models, will be investigated in the rest of this section.

4.1. Can the vector-meson mass be a hard scale ?

Data from photoproduction at HERA permit to test the behaviour of exclusive vector-meson production as a function of the meson mass because $Q^2 = 0$. Figure 8 shows the cross sections for photoproduction of ρ , ω , ϕ , J/Ψ , $\Psi(2S)$, and Υ as functions of W [8, 9, 10, 11, 12, 13]. The lines through the data points are only to guide the eye and are not fit results. The W -dependence of the light vector-mesons (ρ , ω , ϕ) can be described by a slope $\delta \approx 0.22$ in agreement with Regge phenomenology. For higher vector-meson masses, the rise with W gets steeper. This indicates the onset of hard diffraction. Therefore exclusive production of J/Ψ mesons should be described by pQCD model calculations already from $Q^2 = 0$ on. In Fig.9 the photoproduction cross-section for J/Ψ mesons as a function of W is

compared to pQCD model calculations [14]. These calculations are able to describe the data qualitatively. PQCD models predict little or no shrinkage. Figure 10 shows measurements of slope parameters, b , for photoproduction of ρ mesons at different W values. From these measurements one extracts $\alpha' = 0.3 \pm 0.4 \text{ GeV}^{-2}$. Within the large uncertainty this is compatible with the value of 0.25 expected for soft processes. For the photoproduction of J/Ψ -mesons the same is shown in Fig.11. Here one finds $\alpha' = (0.164 \pm 0.028 \pm 0.030) \text{ GeV}^{-2}$ which is smaller than 0.25. This again indicates that photoproduction of J/Ψ mesons is not a soft process and the vector-meson mass can provide a hard scale which makes pQCD applicable.

4.2. Can Q^2 provide a hard scale ?

The cross section for exclusive production of ρ mesons at $Q^2 = 0$ behaves like $\sigma(W) \propto (W/W_0)^\delta$ with $\delta = 0.22$ as shown in section 5.1. Figure 12 shows this cross section as a function of W for higher values of Q^2 [15]. The exponent δ increases with Q^2 as shown in Fig.13. This indicates the transition from a soft process to hard one. In Fig.14, the cross section for J/Ψ productions is shown as a function of W for different Q^2 [16]. The dependence on W hardly changes with Q^2 and already at $Q^2 = 0$ the exponent δ is bigger than 0.22. The δ value for J/Ψ production is approximately equal to the value for ρ production at high Q^2 . Figure 15 shows the cross section for J/Ψ production as a function of Q^2 . The data are well described by pQCD models [17] [18] even from $Q^2 = 0$ on. These models use parton distributions derived from inclusive deep-inelastic scattering (see section 6.7). The slope b of the t distribution is supposed to change in a transition from the Regge regime to pQCD. The Figs.16 and 17 show this slope as a function of Q^2 for ρ and J/Ψ production. For ρ production, the t slope decreases with increasing Q^2 to a value of about 4 as expected from pQCD models. For J/Ψ production this slope is constant with Q^2 at the level of about 4 which reflects the fact that J/Ψ production is a hard process from $Q^2 = 0$ on. One concludes that the initially soft ρ -production becomes a hard process with increasing Q^2 whereas the J/Ψ production is a hard process from $Q^2 = 0$ on.

4.3. Can t provide a hard scale ?

In a similar way as the square of the momentum transfer from the electron to the vector-meson, Q^2 , leads eventually to a hard scale which justifies the application of pQCD one would expect that also the square of the momentum transfer from the proton to the vector-meson, t , can serve as a hard scale. To study this, photoproduction of vector-mesons at high $|t|$ has been investigated. Experimentally, this leads to a small complication.

All studies presented so far have been performed with data integrated over t . Since the differential cross-section is exponentially falling with increasing $|t|$, mainly very small $|t|$ values dominate these data. At higher $|t|$ values, it becomes more and more likely that the proton will dissociate into a hadronic system N , e.g. N being a nuclear resonance, the particles emerging from this system leave the detector under very small angles through the beam pipe without being detected. These events cannot be distinguished experimentally from events in which the proton stays intact. At higher masses of N , some of the particles of the system N emerge with high enough transverse momenta to be seen in the detector. These events can be recognized and excluded from the dataset. Thus at higher $|t|$ values, one deals with a mixture of proton dissociatives and non-dissociative events. At very high $|t|$ values, the proton-dissociative events finally dominate. In order to draw conclusions from such event samples for the process of diffraction one has to assume vertex factorisation, i.e. that the ratio $\sigma_{\gamma p \rightarrow \rho N} / \sigma_{\gamma p \rightarrow \rho p}$ depends only on M_N , W , and t and not on Q^2 . Data on this ratio are shown in Fig.18. Within the experimental uncertainties, vertex factorisation holds.

In Fig.19, $|t|$ distributions are shown for proton-dissociative photo-production of ρ , ϕ , and J/Ψ mesons from ZEUS [19]. The data are well described by fits of the form :

$$\frac{d\sigma_{\gamma p \rightarrow V N}}{dt} \propto |t|^{-n} .$$

The data are fitted to the form $d\sigma/d|t| \propto (-t)^{-n}$. The fit results for the exponents are given in the figure. The data are compared to pQCD models of Bartels et al. [20] and Ivanov et al. [21]. It follows from the above results that also large $|t|$ provides a hard scale.

4.4. The Pomeron Trajectory

Staying within the framework of Regge theory, the best way to determine the pomeron trajectory is to extract $\alpha_P(t)$ from the W dependence of the data in different t bins according to:

$$\frac{d\sigma}{dt} \propto e^{b(W) \cdot t} \left(\frac{W}{W_0} \right)^{4(\alpha_P(t)-1)} .$$

Figure 20 shows the determined pomeron trajectories for photoproduction of ρ , ϕ , and J/Ψ mesons as well as the one from DIS ρ -production.

The following trajectories are derived from the data :

$$\begin{aligned}
\rho \text{ photoproduction} & : \alpha_{\mathbb{P}}(t) = 1.10 + 0.13 \cdot t , \\
\phi \text{ photoproduction} & : \alpha_{\mathbb{P}}(t) = 1.08 + 0.16 \cdot t , \\
\text{DIS } \rho \text{ production} & : \alpha_{\mathbb{P}}(t) = 1.14 + 0.04 \cdot t , \\
J/\Psi \text{ photoproduction} & : \alpha_{\mathbb{P}}(t) = 1.20 + 0.12 \cdot t .
\end{aligned}$$

The $\alpha_{\mathbb{P}}(0)$ values of ρ - and ϕ -photoproduction are compatible with the soft-pomeron trajectory. The $\alpha_{\mathbb{P}}(0)$ values of DIS ρ - and J/Ψ -production are definitely higher.

5. Inclusive deep-inelastic diffraction at HERA

In the Regge picture, inclusive deep-inelastic diffraction at HERA proceeds via the diagram shown in Fig.21, where it is assumed that the pomeron has a partonic structure, following the initial idea of [23]. The exchange of the colourless pomeron leads to a rapidity gap between the outgoing proton, or the proton dissociative system N with a mass M_N , and the diffractively produced system X with mass M_X . In pQCD, successful descriptions of inclusive deep-inelastic diffraction are often formulated in the colour-dipole picture as shown in Fig.22.

5.1. Methods to measure inclusive diffraction

There is no unique definition of a cross section for deep inelastic diffractive scattering. Different methods exist to select diffractive events. These methods select samples which contain different fractions of proton dissociative events. Cross sections are usually given without corrections for proton dissociation. A second problem originates from the fact that also non-diffractive events may contain a rapidity gap due to the statistical nature of fragmentation or from the exchange of reggeons. Such rapidity gaps are, however, exponentially suppressed [22]. Different selection methods may lead to different contributions of non-diffractive events to the selected sample. The following three selection methods have been used to select inclusive diffractive events.

- Detection of the diffractively scattered proton.

The diffractively scattered protons are detected with specialised detector parts like silicon-strip detectors very close to the proton beamline between 20 m and 90 m away from the interaction point. Figure 23 shows a measured spectrum of the longitudinal momentum-fraction of

the detected proton w.r.t. the incoming proton, $x_L = 1 - x_P$. Clearly visible is the diffractive peak around $x_L \approx 1$. Events at lower x_L originate from proton-dissociative diffraction and non-diffractive processes. The detection of the diffractively scattered proton is the only method to measure the t distribution of inclusive diffractive-reactions:

$$t = \frac{-p_T^2}{x_L} - \frac{(1 - x_L)^2}{x_L} m_p^2.$$

This method has the advantage of yielding a diffractive event sample which is practically free of proton dissociation as long as x_P is below 0.01. At higher x_P values, reggeon contributions and proton dissociation may contribute. The disadvantage of the method is its small acceptance and therefore a small number of selected events.

- The rapidity gap method.

The (pseudo)-rapidity of a particle in an event is defined as $\eta = -\ln(\tan(\Theta/2))$, where Θ is the scattering angle of the particle w.r.t. the incoming proton beam. An event-display picture of a diffractive DIS event recorded with the H1 detector is shown in Fig.24. There is a rapidity gap between the proton direction and the final state particle detected under the smallest angle Θ_{min} , respectively η_{max} . Figure 25 is an example of a measured η_{max} distribution from H1. Also shown in the figure as a histogram is the contribution to the data from non-diffractive events. The region below an η_{max} value of about 2 is dominated by diffractive events which show an almost constant behaviour down to small η_{max} values. Applying an η_{max} cut is equivalent to restricting the events to low x_P values because $\eta_{max} \approx \ln(1/x_P)$. This method has the advantage of a large acceptance yielding high statistics data samples. It has the disadvantage that the selected data sample contains in certain kinematical regions contributions from non-diffractive processes and from proton-dissociation events.

- The M_x method.

This method exploits the difference in the shape of the invariant mass distribution of the final state particles seen in the detector for non-diffractive and diffractive events.

(i) In non-diffractive events, the particles are produced evenly distributed in rapidity $y = 1/2 \cdot \ln[(e + p_z)/(e - p_z)]$ between y_{max} and y_{min} . The length of the rapidity plateau is given by the center of mass energy which is W for virtual photon scattering:

$$\ln W^2 \propto y_{max} - y_{min} .$$

However, not all final state particles are seen in the detector. The ones which are produced with $y > y_{limit}$ escape through the forward beam-hole, where y_{limit} is given by the end of the detector acceptance. The particles seen in detector lead to an invariant mass M_x given by W . Therefore

$$W^2 = c_0 \cdot e^{y_{max}-y_{min}} \quad \text{and} \quad M_x^2 = c_0 \cdot e^{y_{limit}-y_{min}} .$$

The value of M_x will fluctuate due to the finite probability that no particles are emitted between y_{limit} and $y_{limit} - \Delta y$. This generates a rapidity gap also in non-diffractive events. The assumption of uncorrelated particle emission leads to a Poissonian rapidity gap distribution, $P(\Delta y) = e^{-\lambda \Delta y}$. This results in an exponential behaviour in the $\ln M_x^2$ distribution of non-diffractive events,

$$\frac{dN}{d\ln M_x^2} = c \cdot e^{b \cdot \ln M_x^2} .$$

The slope parameter b and the normalisation constant c can be determined from measured data.

(ii) For diffractive events, it is known from experiments that at not too low M_x one gets

$$\frac{dN}{dM_x^2} \propto \frac{1}{(M_x^2)^n} \quad \text{with} \quad n \approx 1 \quad \text{or} \quad \frac{dN}{d\ln M_x^2} \approx \text{constant} = D .$$

This can also be derived from a triple-Regge model.

(iii) Measured event samples consist of non-diffractive and diffractive events. This results in a $\ln M_x^2$ distribution of:

$$\frac{dN}{d\ln M_x^2} = D + c \cdot e^{b \cdot \ln M_x^2} .$$

Figure 26 shows a $\ln M_x^2$ distribution measured in the ZEUS experiment for the kinematical region $40 < Q^2 < 50 \text{ GeV}^2$ and $200 < W < 245 \text{ GeV}$. The two components are clearly visible. Shown are also MC simulations of the non-diffractive and the diffractive contributions. The sum of the two contributions describe well the measured data.

(iv) The analytic form of the $\ln M_x^2$ distribution is fitted to the measured distribution over the region indicated by the two vertical lines in Fig.26. For the fit, D is taken to be constant. The fitted parameters

are D , c and the exponential slope b . However, the diffractive contribution is not taken as D but the fitted non-diffractive contribution, as indicated by the dotted line in Fig.26, is statistically subtracted from the measured data. The advantage of the $\ln M_x^2$ method is that it removes non-diffractive background and that its acceptance is high. Like the rapidity-gap method, the $\ln M_x^2$ method allows contributions from proton-dissociative events.

5.2. Diffractive cross-section and diffractive structure-functions

The differential cross-section for diffractive processes is given by:

$$\frac{d^4\sigma}{dQ^2 dt dx_{IP} d\beta} = \frac{2\pi\alpha_{em}}{\beta Q^2} [1 - (1-y)^2] \cdot \sigma_r^{D(4)}(Q^2, t, x_{IP}, \beta)$$

where the reduced cross-section $\sigma_r^{D(4)}(Q^2, t, x_{IP}, \beta)$ is defined as:

$$\sigma_r^{D(4)}(Q^2, t, x_{IP}, \beta) = F_2^{D(4)}(Q^2, t, x_{IP}, \beta) - \frac{y^2}{1 + (1-y)^2} F_L^{D(4)}(Q^2, t, x_{IP}, \beta).$$

Here $F_2^{D(4)}$ and $F_L^{D(4)}$ are the diffractive structure-functions in analogy to F_2 and F_L in inclusive deep-inelastic scattering. The longitudinal contribution becomes sizable only at very high y values. Therefore, the ZEUS collaboration neglects it and assumes $\sigma_r^{D(4)} = F_2^{D(4)}$. If the variable t is not measured but integrated over the cross section is:

$$\frac{d^3\sigma}{dQ^2 dx_{IP} d\beta} = \frac{2\pi\alpha_{em}^2}{\beta Q^4} [1 - (1-y)^2] \cdot \sigma_r^{D(3)}(Q^2, x_{IP}, \beta).$$

In diffractive deep-inelastic scattering, QCD factorisation of the following form has been proven [24]:

$$\sigma^{diff} \propto f_q^{diff}(Q^2, t, x_{IP}, \beta) \cdot \hat{\sigma}_{pQCD}.$$

Here $f_q^{diff}(Q^2, t, x_{IP}, \beta)$ are universal diffractive parton-distributions and $\hat{\sigma}_{pQCD}$ is the perturbatively calculable cross section for the hard parton-parton scattering. Another factorisation is commonly used in the picture where the pomeron has a partonic structure [23]. This is illustrated in Fig.27. Neglecting the longitudinal contribution, the diffractive cross-section is expressed by a pomeron structure-function F_2^{IP} and a pomeron-flux factor which is derived from the triple-Regge formalism:

$$\sigma_{diff} \propto f_{IP/p}(t, x_{IP}) \cdot F_2^{IP}(Q^2, \beta) \quad \text{with} \quad f_{IP/p}(t, x_{IP}) = \frac{e^{B \cdot t}}{x_{IP}^{2\alpha(t)-1}}.$$

This Regge factorization is an assumption. No proof exists for it.

The data selected by the LRG method or by detecting the diffractively scattered proton may contain contributions from reggeon exchanges which are non-diffractive. Therefore the results are fitted to a sum of a pomeron and of a reggeon contribution:

$$F_2^{D(4)}(x_{IP}, t, \beta, Q^2) = f_{IP}(x_{IP}, t) \cdot F_2^{IP}(\beta, Q^2) + n_{IR} f_{IR}(x_{IP}, t) \cdot F_2^{IR}(\beta, Q^2).$$

For $F_2^{IR}(\beta, Q^2)$ the pion structure-function is used and the flux factors for pomeron and reggeon exchanges are parametrised as given in the previous section. The fluxes are normalised according to $x_{IP} \cdot \int_{-1}^{t_{min}} f_{IP/IR}(x_{IP}, t) = 1$ at $x_{IP} = 0.003$ with $|t_{min}| \approx m_p^2 x_{IP}^2 / (1 - x_{IP})$. The main fit results are $F_2^{IP}(\beta, Q^2)$ and n_{IR} , the relative normalisation of the reggeon contribution. Other parameters, like $\alpha_{IP/IR}(0)$, $\alpha'_{IP/IR}(0)$, $B_{IP/IR}$ are either also fitted or taken from other measurements. The above described fitting procedure can be performed as well if t has not been measured but averaged over. In this case the flux factors are also averaged over t .

In a picture in which the pomeron has a partonic structure, $F_2^{IP}(\beta, Q^2)$ can be interpreted as the pomeron structure-function, very much like $F_2(\beta, Q^2)$ as the proton structure-function. Analogously it can be expressed as a sum of universal pomeron parton-distribution functions (pdf):

$$F_2^{IP}(\beta, Q^2) = \sum_i f_i^D(\beta, Q^2)$$

where i denotes the parton species: u, d, s, gluon and the respective anti-partons. In pQCD, these pomeron pdfs should obey the DGLAP evolution. DGLAP fits and Regge fits are usually carried out simultaneously.

5.3. Results from the proton detection method

The H1 and the ZEUS experiments both are equipped with detector components very close to the proton beam at a distance of up to 90 m downstream of the experiment in proton direction: the forward proton spectrometer, FPS (H1), and the leading proton spectrometer, LPS (ZEUS). These spectrometers detect protons at high x_L . Results for $x_{IP} \sigma_r^D(3)$ from H1 [25] are shown in Fig.28 and for $x_{IP} F_2^{D(4)}$ at two different t -values from ZEUS [26] are presented in Fig.29 as functions of x_{IP} for different Q^2 and β values. In general, the data rise with decreasing x_{IP} for $x_{IP} < 0.01$. In both experiments one sees a rise of the data at high x_{IP} due to onset of reggeon contributions.

5.4. Results from the large rapidity gap method

The results from the large rapidity-gap method for inclusive diffraction from H1 [27] and ZEUS [26] are shown in Fig.30 and Fig.31. The reduced cross section, $x_{IP}\sigma_r^{D(3)}$, or the diffractive structure-function, $x_{IP}F_2^{D(3)}$, are displayed as functions of x_{IP} for different values of Q^2 and β . The results from both experiments show qualitatively the same features. For not too low β , they rise towards low x_{IP} for $x_{IP} < 0.01$. At higher x_{IP} , they may rise again slightly which is due to reggeon contributions. The H1 and ZEUS data agree in shape. A quantitative comparison has to take into account the different contents of proton dissociation in the data.

5.5. H1 fits of the diffractive parton distributions

As explained in 6.2, under the assumption of Regge factorisation, one can define universal diffractive parton-distributions (dpdf), f_i . The H1 collaboration fitted the dpdfs to the following parametrisation at Q_0^2 :

$$zf_i(z, Q_0^2) = A_i z^{B_i} (1 - z)^{C_i} \cdot e^{-\frac{0.01}{1-z}}.$$

Here z is the longitudinal momentum-fraction of the parton entering the hard sub-process. For the lowest order quark-parton model process $z = \beta$, for higher order processes $0 < \beta < z$. The index i stands for the different quark flavours and the gluon. For data with $Q^2 > 8.5 \text{ GeV}^2$ two different fits were performed [27]:

- Fit A: $Q_0^2 = 1.75 \text{ GeV}^2$ and B_{gluon} was set to zero;
- Fit B: $Q_0^2 = 2.50 \text{ GeV}^2$ and B_{gluon} and C_{gluon} were set to zero.

Both fits gave similar results, except for the diffractive gluon-distribution at lower Q^2 and high z . Figure 32 shows the results of the fits for the singlet and gluon dpdfs.

5.6. Results from the $\ln M_x^2$ -method and the BEKW(mod) fit

The ZEUS collaboration measured inclusive diffraction at HERA with the $\ln M_x^2$ -method [28]. Their results for $x_{IP}F_2^{D(3)}$ as a function of x_{IP} for different Q^2 and β values are given in Fig.34. Also here, the clear rise of $x_{IP}F_2^{D(3)}$ with decreasing x_{IP} is visible. The lines are the results of a modified BEKW fit. The BEKW model [29] is a coloured-dipole model. The model takes into account terms from transverse photons, $(F_{q\bar{q}}^T)$, and longitudinal photons, $(F_{q\bar{q}}^L)$. In addition it contains a contribution, $(F_{q\bar{q}g}^T)$,

from the splitting of the the virtual photon in a $q\bar{q}g$ state which interacts with the photon. These three terms are parametrized in the following way:

$$x_{IP}F_2^{D(3)}(\beta, x_{IP}, Q^2) = c_T \cdot F_{q\bar{q}}^T + c_L \cdot F_{q\bar{q}}^L + c_g \cdot F_{q\bar{q}g}^T,$$

where

$$\begin{aligned} F_{q\bar{q}}^T &= \left(\frac{x_0}{x_{IP}} \right)^{n_T(Q^2)} \cdot \beta(1 - \beta), \\ F_{q\bar{q}}^L &= \left(\frac{x_0}{x_{IP}} \right)^{n_L(Q^2)} \cdot \frac{Q_0^2}{Q^2 + Q_0^2} \cdot \left[\ln \left(\frac{7}{4} + \frac{Q^2}{4\beta Q_0^2} \right) \right]^2 \cdot \beta^3(1 - 2\beta)^2, \\ F_{q\bar{q}g}^T &= \left(\frac{x_0}{x_{IP}} \right)^{n_g(Q^2)} \cdot \ln \left(1 + \frac{Q^2}{Q_0^2} \right) \cdot (1 - \beta)^\gamma. \end{aligned}$$

For $F_{q\bar{q}}^L$, the term $(\frac{Q_0^2}{Q^2})$ provided by BEKW was replaced by the factor $(\frac{Q_0^2}{Q^2 + Q_0^2})$ to avoid problems as $Q^2 \rightarrow 0$. The powers $n_{T,L,g}(Q^2)$ were assumed by BEKW to be of the form $n(Q^2) = n_0 + n_1 \cdot \ln[1 + \ln(\frac{Q^2}{Q_0^2})]$. The present data suggested using the form $n(Q^2) = n_0 + n_1 \ln(1 + \frac{Q^2}{Q_0^2})$. This modified BEKW form will be referred to as BEKW(mod). Taking $x_0 = 0.01$ and $Q_0^2 = 0.4 \text{ GeV}^2$, the BEKW(mod) form gives a good description of the data. According to the fit, the coefficients n_0 can be set to zero, and the coefficient n_1 can be assumed to be the same for T , L and g . Figure 33 shows the measured $x_{IP}F_2^{D(3)}$ values for $Q^2 = 25 - 320 \text{ GeV}^2$ as a function of β . Also given are the transverse, longitudinal and $q\bar{q}g$ contributions from the fit. For $x_{IP} = 0.01$, the dependence of $F_2^{D(3)}$ is shown in Fig.34 for all Q^2 values together with the BEKW(mod) fit results. The data points from all Q^2 values fall approximately on the same curve. The broad maximum around $\beta = 0.5$ is explained by the transverse contribution which reflects the $\beta(1 - \beta)$ behaviour of the $q\bar{q}$ component. For small β values the data start to rise rapidly which is explained by the rise of the $q\bar{q}g$ contribution. The indication of a rise of the data towards very high β may be explained by the onset of the longitudinal contribution.

In Fig.35, the measured $x_{IP}F_2^{D(3)}$ values are plotted as a function of Q^2 for $x_{IP} = 0.01$ and different β values. The lines are the results of the BEKW(mod) fit. One sees clearly a pattern of scaling violation similar to that of the F_2 in deep-inelastic scattering. The ZEUS data are compared to the results from H1 measured with the LRG method. For this comparison the H1 binning has been chosen and only those data from ZEUS are shown which could be translated to this binning with a correction of less than 20%. There is fair agreement between the H1 and ZEUS data.

6. Semi-inclusive deep-inelastic diffraction at HERA

Semi-inclusive deep-inelastic diffractive reactions are a good testing ground for the universality of diffractive parton-distributions derived from inclusive diffractive reactions. So far the production of D^* mesons and of two jets in the final state of diffractive reactions have been studied.

The diffractive production of $D^*(2010)$ mesons proceeds via the process depicted in Fig.36. The $c\bar{c}$ quark-pair from the photon-gluon fusion forms the D^* meson which decays into $D^0\pi$ and successively into $K\pi\pi$. The D^* is detected as a peak in the distribution of the mass difference $M(K\pi\pi) - M(K\pi)$ where $M(K\pi)$ is in the mass region of D^0 meson, as shown in Fig.37. Figure 38 shows results from ZEUS [30] for the semi-inclusive diffractive $D^*(2010)$ production for several differential cross sections. The solid line is a NLO QCD calculation for that process using diffractive parton-distributions which have been determined from combined H1 and ZEUS data (ATCW fit) [31]. The dashed line is a MC-simulation using the SATRAP generator which is based on a colour-dipole model. The NLO QCD calculation is in fair agreement with the data. This confirms the universality of the diffractive parton-distributions.

The semi-inclusive diffractive DIS production of two jets takes place via photon-gluon fusion and the produced quark and antiquark form a jet each. Figure 39 presents results of H1 [32] on differential cross sections of diffractive 2-jet production. The data are compared to NLO QCD calculations using the H1 fits A and B. The calculation describes reasonably well the data. This is another confirmation of the universality of the diffractive parton-distributions.

The measurements of semi-inclusive diffractive 2-jet production enable a combined QCD fit of the diffractive parton-distributions using these results together with the results for inclusive diffraction. Figure 40 shows the combined fits made by the H1 collaboration with their data at $Q^2 = 25 \text{ GeV}^2$ and $Q^2 = 90 \text{ GeV}^2$. The singlet distribution-functions are hardly changed by the combined fits. The additional 2-jet data have an impact on the gluon distributions. The combined fit result is closer to the old H1 fit B.

7. Predictions from the HERA diffractive parton-distributions for Tevatron data

The fact that predictions of semi-inclusive diffractive processes using the the diffractive parton-distributions from inclusive diffractive-processes are in agreement with the data from HERA within the uncertainties raises the question how universal such parton distributions are. Can one use them to predict diffractive processes in proton-antiproton scattering? Diffractive 2-jet cross sections have been measured at the Tevatron [33]. The main

contribution to this process proceeds according to the diagram shown in Fig.41. A gluon from the proton (antiproton) and a gluon originating from a pomeron emitted by the antiproton (proton) collide and form two jets with a rapidity gap in the event. This process is described by two structure functions, one of which is a diffractive one:

$$\sigma(\bar{p}p \rightarrow \bar{p}X) \propto F_{jj} \otimes F_{jj}^D \otimes \hat{\sigma}(ab \rightarrow jj).$$

A determination of $F_{jj}^D(\beta)$ by the CDF collaboration from Tevatron data is presented in Fig.42 together with the predictions based on the diffractive parton-distributions from the H1 fit A and H1 fit B. The data are a factor of 5 to 7 lower than the predictions. This is not unexpected because the QCD factorisation has not been proven for hadron-hadron scattering. In diffractive hadron-hadron scattering, interactions between the proton remnant and the pomeron remnant can occur. Particles from such interactions can fill the rapidity gap. This leads to a gap survival probability less than one.

REFERENCES

- [1] T.Regge, Nuov.Cim.14 (1959) 951; Nuov.Cim **18** (1960) 947
- [2] P.Collins, "An Introduction to Regge Theory and High Energy Physics", Cambridge University Press, Cambridge (1977), and references therein.
- [3] G.Chew,S.Frautschi, Phys.Rev.Lett. **7** (1961) 394;
N.Gribov, Sov.Phys.JETP **14** (1962) 478 ; ibid. 1395.
- [4] A Proposal for a Large Electron-Proton Colliding Beam Facility at DESY, DESY HERA 81-10 (1981).
- [5] A.Donnachi and P.V.Landshoff, Nucl.Phys. **B244** (1984) 322 ;
A.Donnachi and P.V.Landshoff, Phys.Lett. **B296** (1992) 227.
- [6] L.N.Lipatov, Sov.J.Nucl.Phys. **23** (1976) 338 ;
E.A.Kuraev, L.N.Lipatov and V.S.Fadin, Sov.Phys.JETP **45** (1977) ;
Y.Y.Balitsky and L.N.Lipatov, Sov.J.Nucl.Phys. **28** (1978) 822.
- [7] J.J.Sakurai, "Currents and Mesons", University of Chicago Press, Chicago (1969);
H.Fraas and D.Schildknecht, Nucl.Phys. **B14** (1969) 543.
- [8] C. Berger et al., Phys. Lett. **39B** (1972) 659;
SWT Collab., Y. Eisenberg et al., Phys. Rev. **D5** (1972) 15;
J. Park et al., Nucl. Phys. **B36** (1972) 404;
SBT Collab., J.Ballam et al., Phys. Rev. **D5** (1972) 545;
SBT Collab., J.Ballam et al., Phys. Rev. **D7** (1973) 3150;
G.E. Gladding et al., Phys. Rev. **D8** (1973) 3721;
W. Struczinski et al., Nucl. Phys. **B108** (1976) 45;

- R. M. Egloff et al, Phys. Rev. Lett. **43** (1979) 657.
 OMEGA Photon Collab., D. Aston et al., Nucl. Phys. **B209** (1982) 56;
 H1 Collab., S. Aid et al., Nucl.Phys. **B463** (1996) 3;
 ZEUS Collab., J.Breitweg et al., Eur.Phys.J. **C2** (1998) 247.
- [9] H.R. Crouch et al., Phys. Rev. **155** (1967) 1468;
 ABBHHM Collab., R. Erbe et al., Phys. Rev. **175** (1968) 1669;
 M. Davier et al., Phys. Rev. **D1** (1970) 790;
 SWT Collab., Y. Eisenberg et al., Phys. Rev. **D5** (1972) 15;
 SBT Collab., J. Ballam et al., Phys. Rev. **D7** (1973) 3150;
 W. Struczinski et al., Nucl. Phys. **B108** (1976) 45;
 R.M. Egloff et al., Phys. Rev. Lett. **43** (1979) 1545 and **44** (1980) 690 (Erratum);
 A.M. Breakstone et al., Phys. Rev. Lett. **47** (1981) 1782;
 D. Aston et al., Nucl. Phys. **B209** (1982) 56;
 LAMP2 Group, D.P. Barber et al., Z. Phys. **C26** (1984) 343;
 OMEGA Collab., M. Atkinson et al., Nucl. Phys. **B231** (1984) 15;
 J. Busenitz et al., Phys. Rev. **D40** (1989) 1.
- [10] J. Busenitz et al., Phys. Rev. **D40** (1989) 1;
 R. Erbe et al., Phys. Rev. **175** (1968) 1669;
 C. Berger et al., Phys. Lett. **B39** (1972) 659;
 J. Ballam et al., Phys. Rev. **D7** (1973) 3150;
 H.J. Besch et al., Nucl. Phys. **B70** (1974) 257;
 H.J. Behrend et al., Phys. Lett. **B56** (1975) 408;
 D.P. Barber et al., Phys. Lett. **B79** (1978) 150;
 D. Aston et al., Nucl. Phys. **B172** (1980) 1;
 M. Atkinson et al., Z. Phys. **C27** (1985) 233;
 ZEUS Collab., M. Derrick et al., Phys.Lett. **B73** (1996) 259.
- [11] B. Knapp et al., Phys. Rev. Lett. **34** (1975) 1040;
 U. Camerini et al., Phys. Rev. Lett. **35** (1975) 483;
 B. Gittelman et al., Phys. Rev. Lett. **35** (1975) 1616;
 T. Nash et al., Phys. Rev. Lett. **36** (1976) 1233;
 BFP Collab., A.R. Clark et al., Phys. Rev. Lett. **43** (1979) 187;
 EMC Collab., J.J. Aubert et al., Nucl. Phys. **B213** (1983) 1;
 NA14 Collab., R. Barate et al., Z. Phys. **C33** (1987) 505;
 E687 Collab., P.L. Frabetti et al., Phys. Lett. **B316** (1993) 197;
 NMC Collab., M. Arneodo et al., Phys. Lett **B332** (1994) 195;
 E401 Collab., M. Binkley et. al., Phys Rev. Lett. **48** (1982) 73;
 E516 Collab., B.H. Denby et al., Phys. Rev. Lett. **52** (1984) 795;
 H1 Collab., S.Aid et al., Nucl.Phys. **B468** (1996) 3;
 ZEUS Collab., J.Breitweg et al., Z.Phys. **C75** (1997) 215;
 ZEUS Collab., S.Chekanov et al., Eur.Phys.J. **C24** (2002) 345;
 H1 Collab., C.Adloff et al., Phys.Lett. **B483** (2000) 23;
 H1 Collab., C.Adloff et al., Contribution to DIS 2003, St.Petersburg, Russia.
- [12] H1 Collab., C.Adloff et al., Phys.Lett. **B541** (2002) 251;
 ZEUS Collab., Contribution to International Europhysics Conference on High Energy Physics, July 2001, Budapest, Hungary.

- [13] H1 Collab., C.Adloff et al., Phys.Lett. **B483** (2000) 23;
ZEUS Collab., J.Breitweg et al., Phys.Lett. **B437** (1998) 432.
- [14] L.Frankfurt, M.McDermott and M.Strikman, Journal of High Energy Physics 103 (2001) 45;
CTEQ Collab., H.L.Lai et al., Eur.Phys.J. **C12** (2000) 375;
A.D.Martin et al., Eur.Phys.J. **C4** (1998) 463.
- [15] Zeus Collab., S.Chekanov et al.,PMC Physics A 2007 **1**,6.
- [16] ZEUS Collab., S.Chekanov et al., Nucl.Phys. **B695**(2004) 3.
- [17] A.D.Martin, M.G.Ryskin and T.Teubner, Phys.Rev. **D62** (2000) 14022;
CTEQ Collab., H.L.Lai et al., Eur.Phys.J. **C12** (2000) 375.
- [18] L.Frankfurt, W.Koepf and M.Strikman, Phys.Rev. **D57** (1998) 512.
- [19] ZEUS Collab., S.Chekanov et al.,Eur.Phys.J. **C26** (2003) 389.
- [20] J.Bartels et al., Phys.Lett. **B375** (1996) 301.
- [21] D.Yu.Ivanov, Phys.Lett. **B478** (2000) 101;
D.Yu.Ivanov, Phys.Rev. **D53** (1996) 3564.
- [22] R.P.Feynman, "Photon-Hadron-Interactions", Benjamin, N.Y. (1972), lectures 50-54.
- [23] G.Ingelman, P.Schlein, Phys.Lett. **B152** (1985) 256.
- [24] J.Collins, Phys.Rev. **D57** (1998) 3051 and erratum-ibid. **D62** (2000) 19902.
- [25] H1 Collab., A.Aktas et al., Eur.Phys.J. **C48** (2006) 749
- [26] L.Lukasik, Measurement of diffractive structure functions with the LRG method and using the leading proton spectrometer at SEUS, Proc. of 15th Int. Workshop on Deep-Inelastic Scattering and Related Subjects, Munich, Germany, April 2007;
L.Lukasik, Inclusive diffraction in DIS, Proc. of the European Physical Society HEP2007, Manchester, England, 19-25 July 2007.
- [27] H1 Collab., A.Aktas et al., Eur.Phys.J. **C48** (2006) 715
- [28] Zeus Collab.,M.Derrick et al., Z.Phys. **C70** (1996) 391;
Zeus Collab., J.Breitweg et al., Eur.Phys.J. **C6** (1999) 43. ZEUS Collab., DESY 08-011, arXiv:0802.3017, submitted to Nucl. Phys. B.
- [29] J.Bartels, J.Ellis, H.Kowalski, M.Wuesthoff, Eur.Phys.J. **C7** (1999) 443.
- [30] ZEUS Collab., S.Chekanov et al., Eur. Phys. J. **C51** (2007)301-315.
- [31] L.Alvero,J.C.Collins,J.Terron and J.J.Whitmore, Phys.Rev. **D59**(1999)074022.
- [32] H1 Collab., A.Aktas et al., JHEP 0710:042 2007.
- [33] CDF Collab., T.Affolder et al., Phys.Rev.Lett. **84** (2000) 5043.

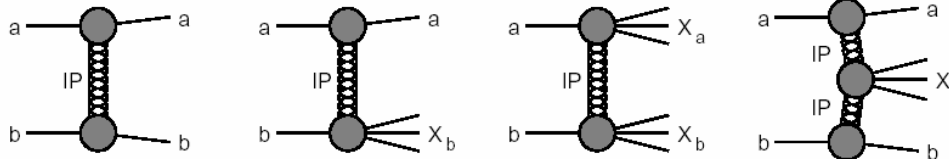


Fig. 1. Diffractive scattering by Pomeron exchange showing from left to right: elastic scattering, single dissociative diffraction, double dissociative diffraction, two Pomeron-exchange diffraction.

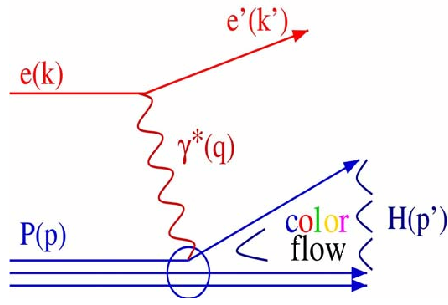


Fig. 2. Diagram for inclusive deep inelastic e-p scattering

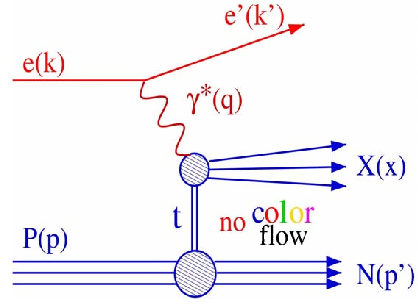


Fig. 3. Diagram for inclusive diffractive e-p scattering

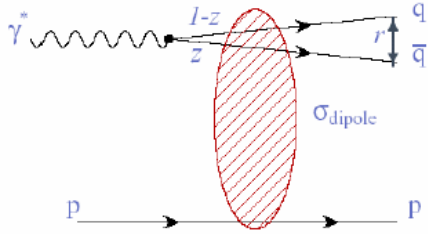


Fig. 4. Diffractive DIS in the colour-dipole picture.

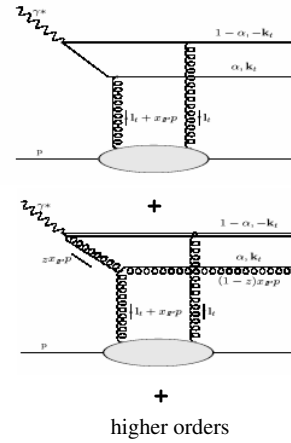


Fig. 5. Diffractive DIS in the colour-dipole model in pQCD.

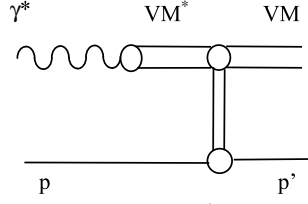


Fig. 6. Exclusive vector-meson production in the VMD-Regge framework.

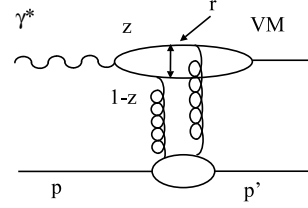


Fig. 7. Exclusive vector-meson production as a pQCD process.

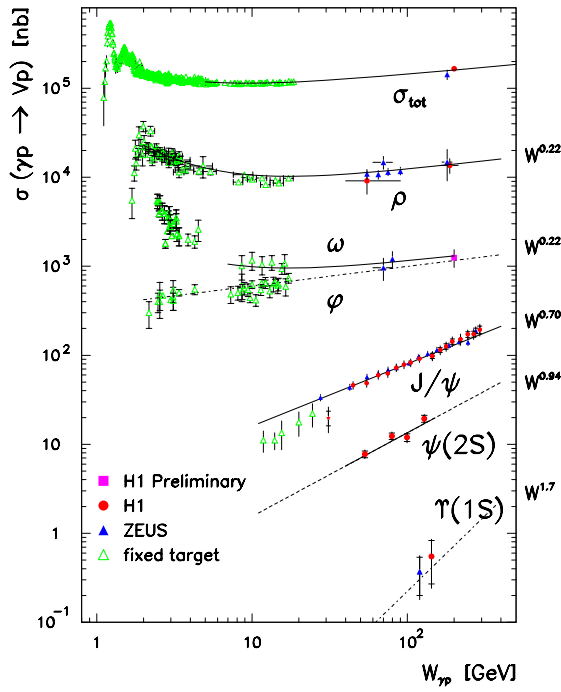


Fig. 8. Photoproduction cross-section for ρ , ω , ϕ , J/Ψ , $\Psi(2S)$, and Υ .

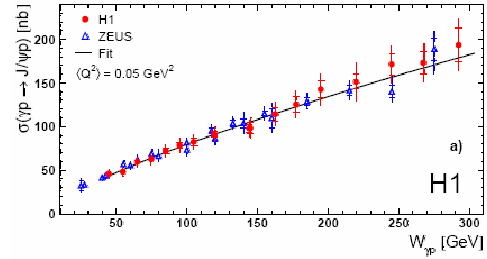


Fig. 9. Cross-section of J/Ψ photoproduction as a function of W compared to pQCD models.

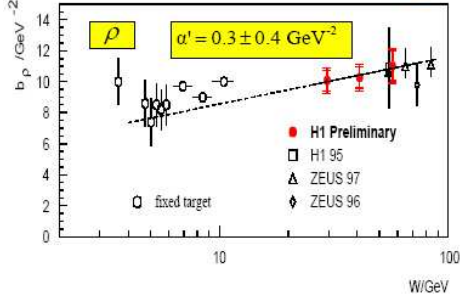


Fig. 10. Slopes of the t dependence for photoproduction of ρ mesons.

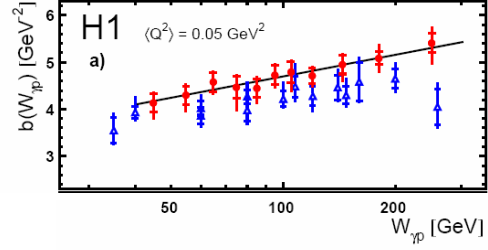


Fig. 11. Slopes of the t dependence for photoproduction of J/Ψ mesons.

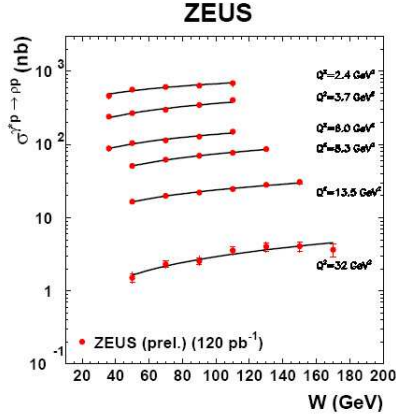


Fig. 12. The W dependence of DIS ρ -production for different values of Q^2 .

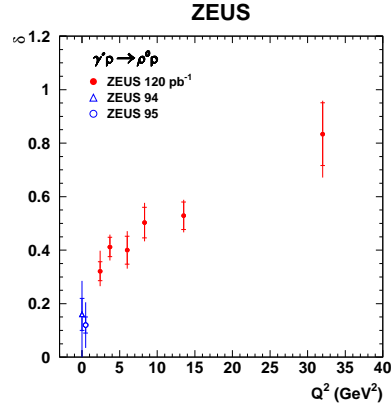


Fig. 13. The slope δ of the W dependence of DIS ρ -production.

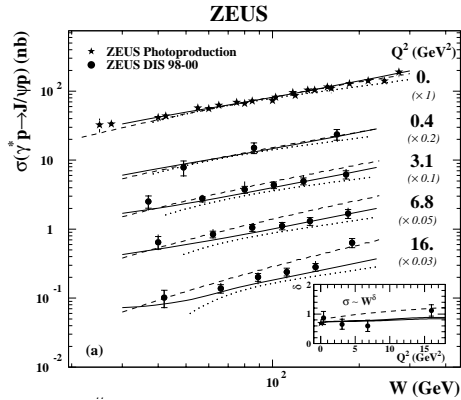


Fig. 14. The W dependence of DIS J/Ψ -production for different values of Q^2 .

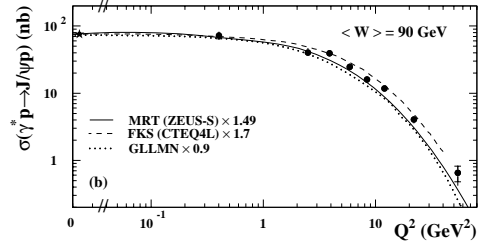


Fig. 15. The Q^2 dependence of DIS J/Ψ -production for different values of Q^2 . See the text for the fits.

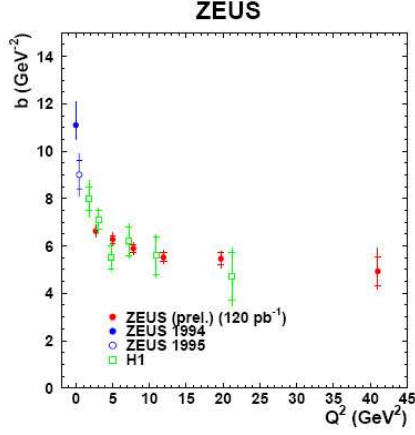


Fig. 16. The t slope parameter b of DIS ρ -production as a function of Q^2 .

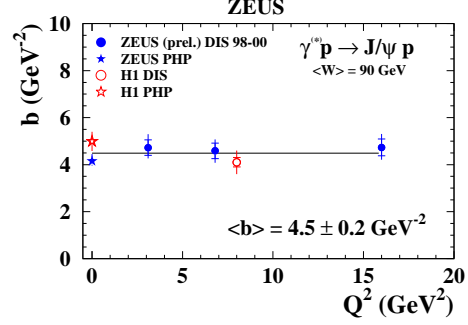


Fig. 17. The t -slope parameter b of DIS J/Ψ -production as a function of Q^2 .

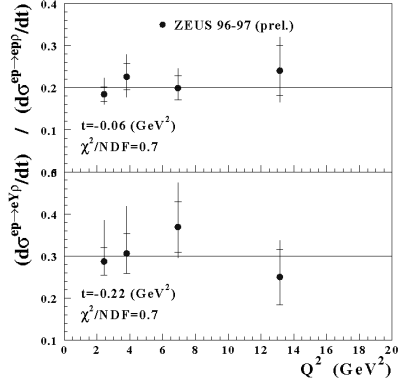


Fig. 18. The ratio of proton dissociative to proton non-dissociative cross sections for DIS ρ -production at $t = -0.06 \text{ GeV}^2$ and $t = -0.22 \text{ GeV}^2$.

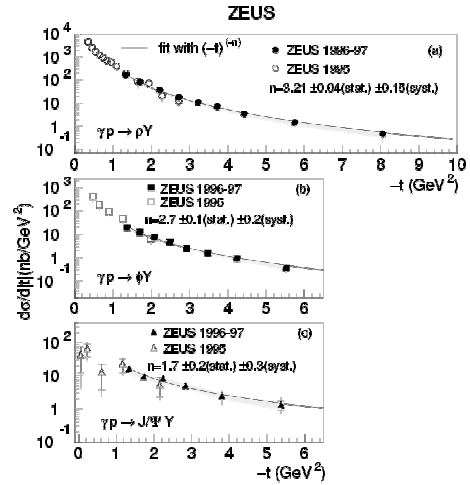


Fig. 19. Differential cross-section as a function of t for proton dissociative photoproduction of ρ, Φ and J/Ψ mesons from the ZEUS experiment.

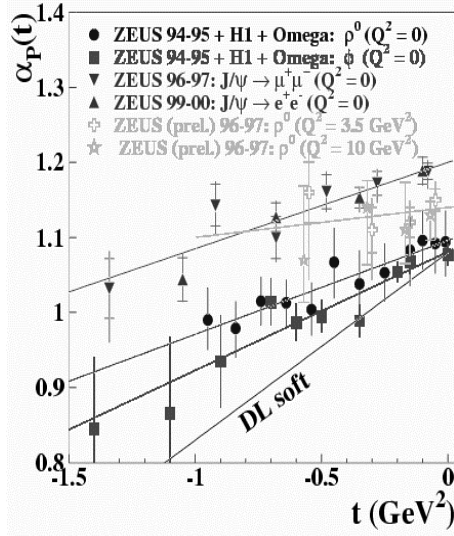


Fig. 20. Pomeron trajectories derived from vector-meson production and soft hadronic processes.

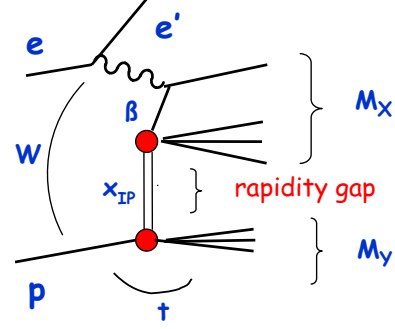


Fig. 21. Schematic diagram for inclusive diffractive scattering in the Regge picture.

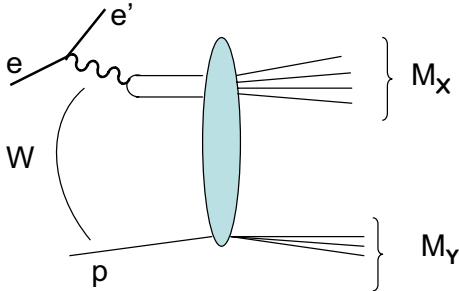


Fig. 22. Schematic diagram for inclusive diffractive scattering in the colour-dipole picture.

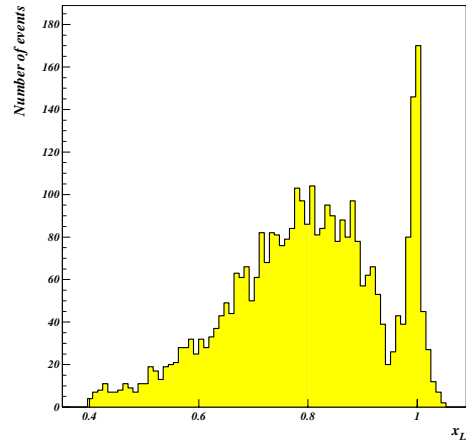


Fig. 23. Fraction x_L of the incoming proton momentum carried by the diffractively scattered proton.

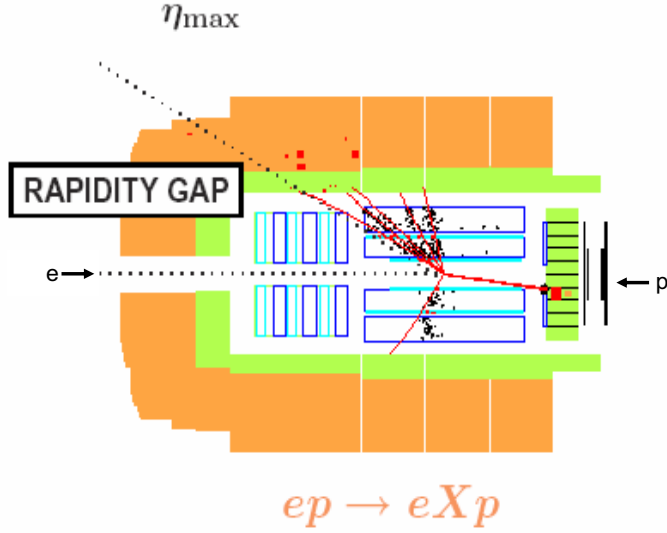


Fig. 24. A diffractive event with a rapidity gap as seen in the H1 detector.

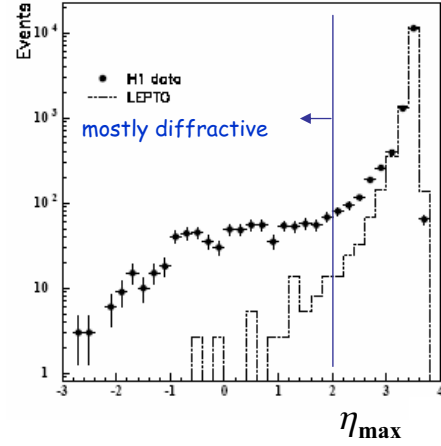


Fig. 25. Measured η_{\max} distribution. Shown as a histogram is the expected contribution from non-diffractive events as simulated by then LEPTO MC generator.

ZEUS

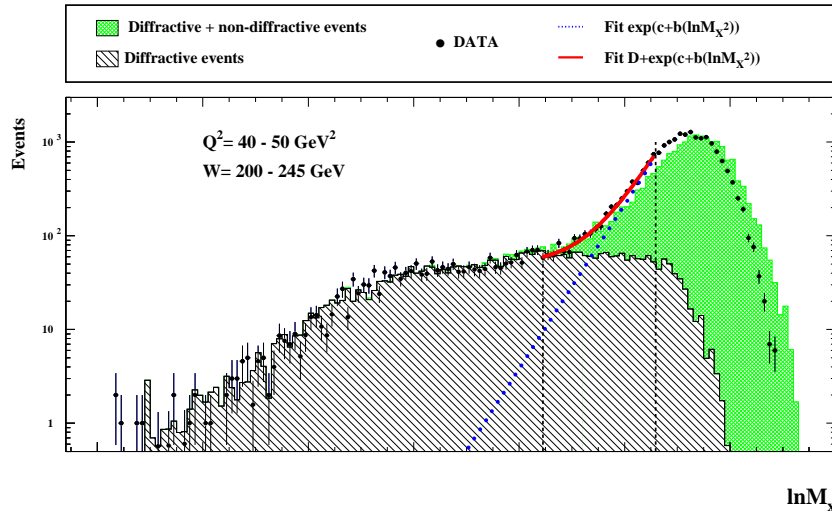


Fig. 26. A measured $\ln M_x^2$ distribution. Also shown are MC simulations of non-diffractive events (cross hatched) and of diffractive events (hatched). The analytic form of the distribution is fitted to the data between the two vertical lines and the fitted slope of the non-diffractive part is shown as a dotted line.

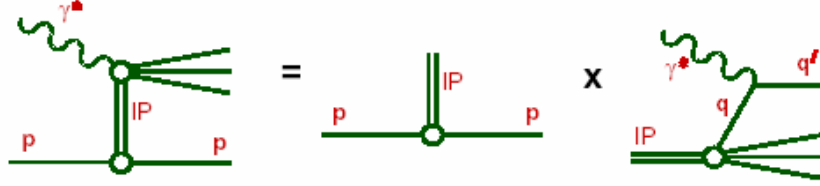


Fig. 27. Schematic picture of Regge factorization.

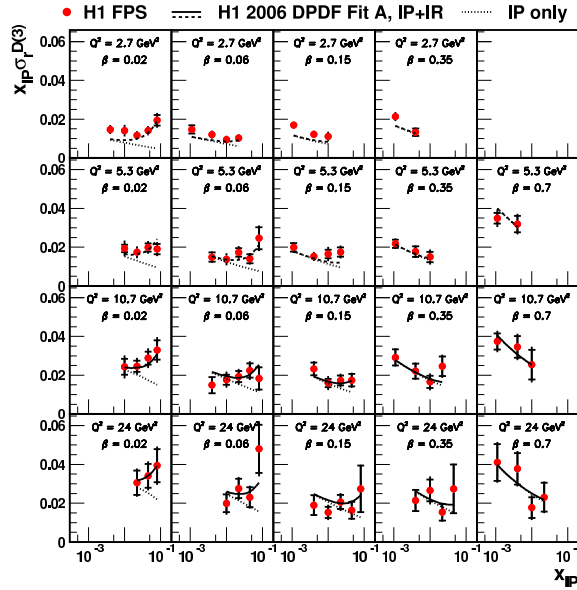


Fig. 28. H1 FPS-results for $x_{IP}\sigma_r^{D(3)}$. The full lines are the result of a combined Regge- and DGLAP-fit, the dashed line is an extrapolation to nonmeasured regions, the dotted lines are the Pomeron contributions only.

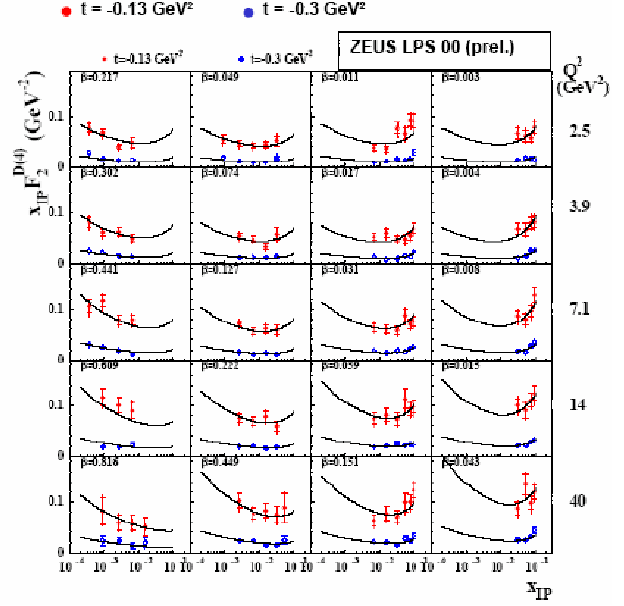


Fig. 29. ZEUS LPS results for $x_{IP}F_2^{D(4)}$ at $t = 0.13 \text{ GeV}^{-2}$ and $t = 0.3 \text{ GeV}^2$. The lines are the result of a combined Regge- and DGLAP-fit.

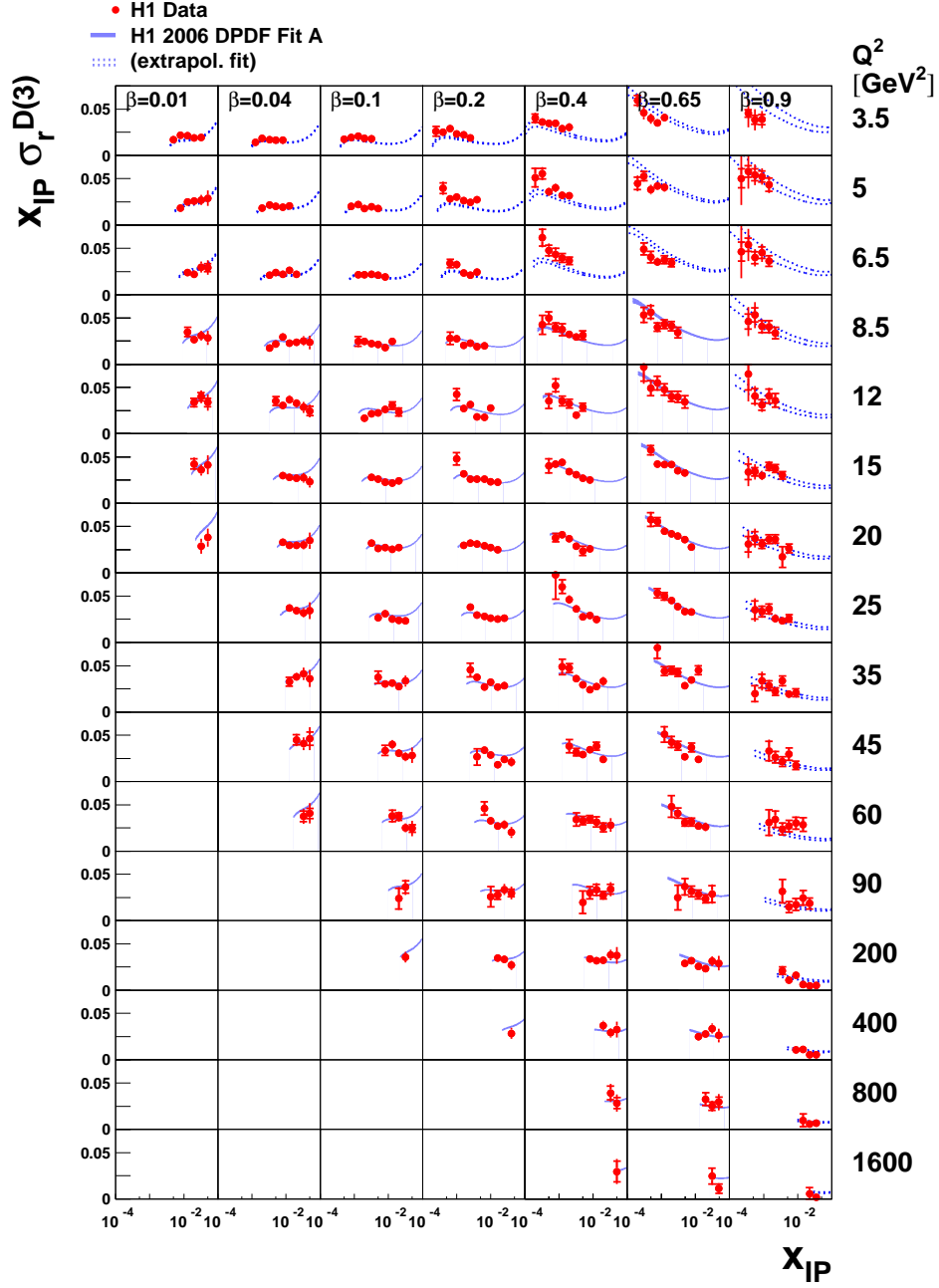
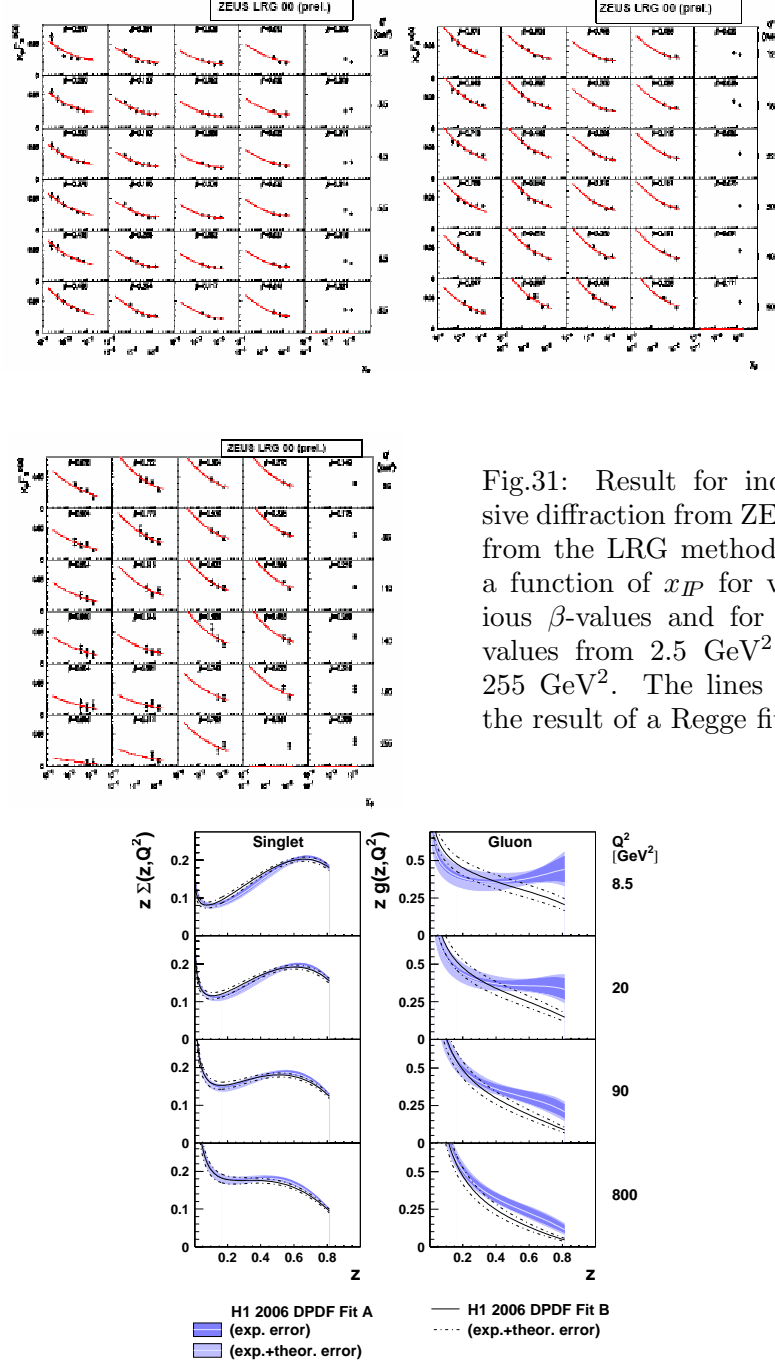


Fig. 30. Results for inclusive diffraction from H1 from the LRG method. The lines are the result of a Regge fit.



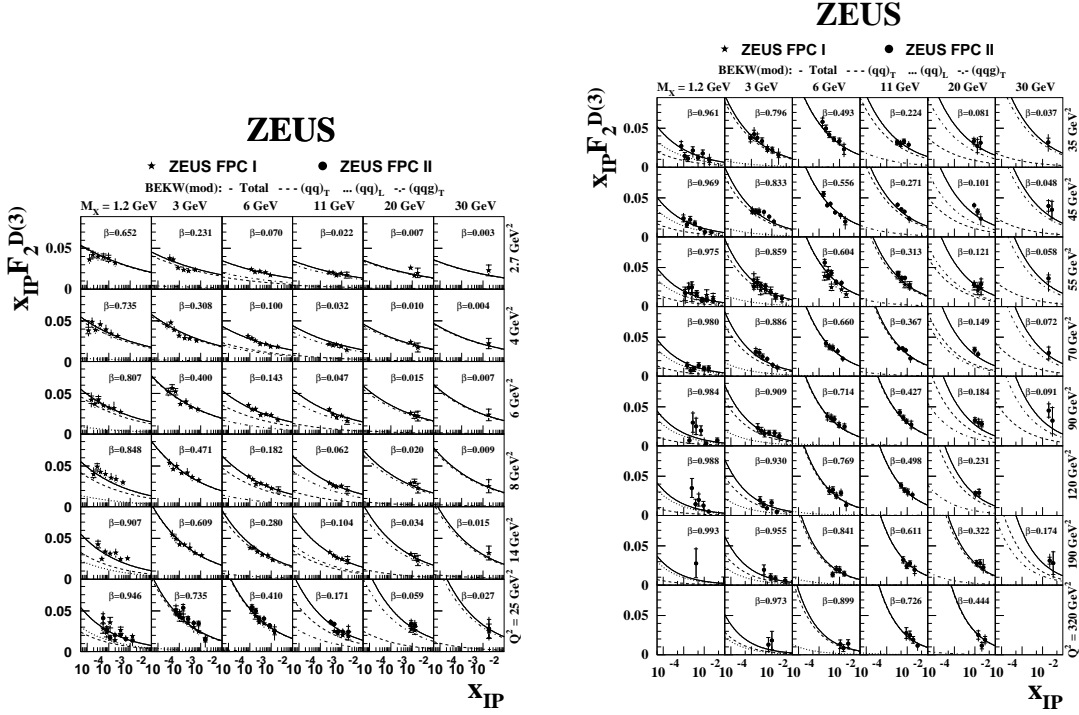


Fig. 33. ZEUS results for $x_{IP} F_2^D(3)$ from the $\ln M_x^2$ -method as a function of x_{IP} at various β -values for Q^2 -values from 2.7 GeV^2 to 25 GeV^2 (left) and from 35 GeV^2 to 320 GeV^2 (right). The lines are the result of a BEKW fit (see text). The solid line is the sum of all contributions, the dashed line is the transverse $q\bar{q}$ contribution, the dotted line is the longitudinal $q\bar{q}$ contribution, and the dashed-dotted line is the $q\bar{q}g$ contribution.

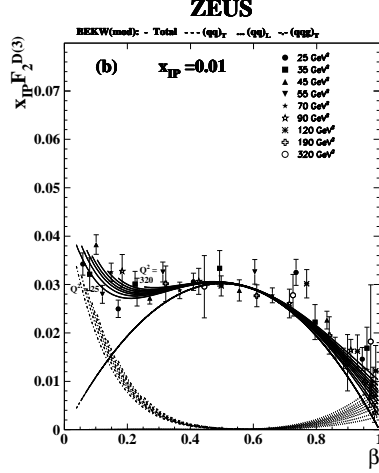


Fig. 34. ZEUS results for $x_{IP} F_2^D(3)$ from the $\ln M_x^2$ -method as a function of β at $x_{IP} = 0.01$ for Q^2 values from 25 GeV² to 320 GeV². The data are compared to the results of the BEKW(mod) fit showing separately the different fit contributions.

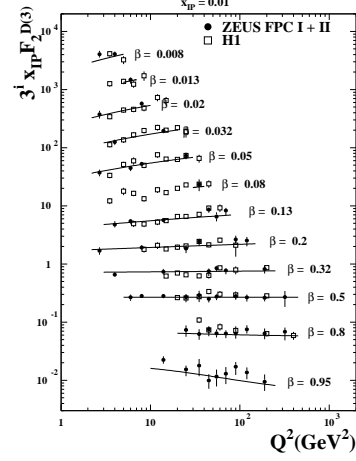


Fig. 35. Comparison of the ZEUS results from the $\ln M_x^2$ -method with the H1 results from the LRG method. Shown are $x_{IP} F_2^D(3)$ values as functions of Q^2 for different β values at $x_{IP} = 0.01$ multiplied by powers of 3 for better visibility. The curves show the results of the BEKW(mod) fit to the ZEUS data.

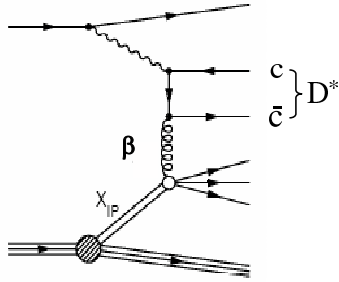


Fig. 36. Graphical presentation of the semi-inclusive diffractive D^* production.

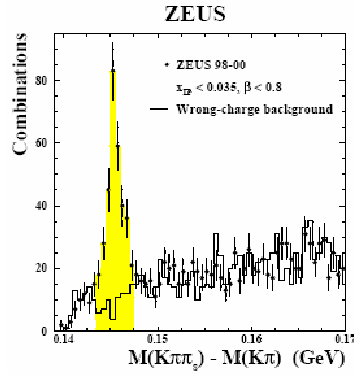


Fig. 37. The signal of the $D^*(2010)$ in the spectrum of the mass difference $M(K\pi\pi) - M(K\pi)$.

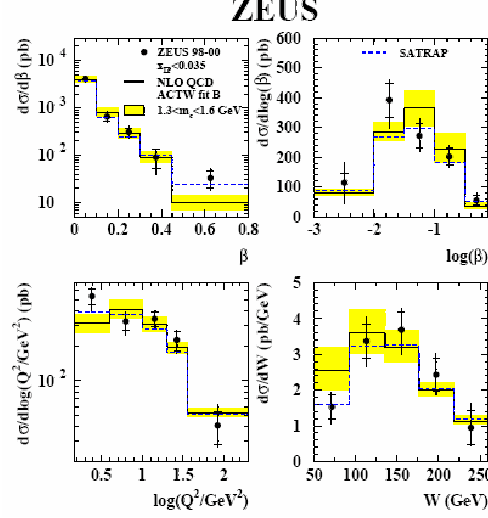


Fig. 38. Differential cross sections for the semi-inclusive diffractive $D^*(2010)$ production. The solid line is a NLO QCD calculation for that process using diffractive parton distribution functions which have been determined from combined H1 and ZEUS data (ATCW fit). The dashed line is a MC-simulation using the SATRAP generator which is based on a colour-dipole model.

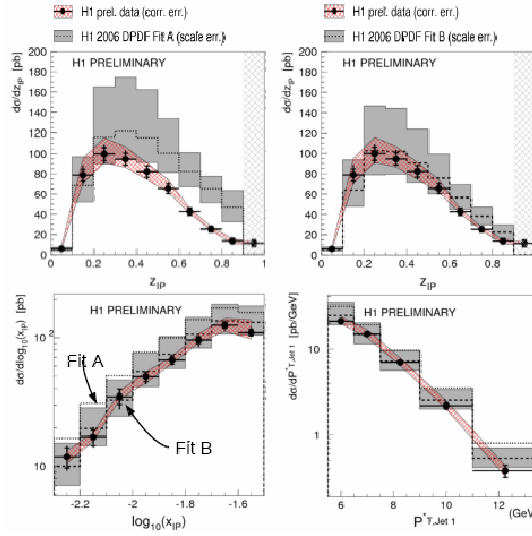


Fig. 39. Differential cross sections for the semi-inclusive 2-jet production from H1. The data are compared to NLO QCD calculations using H1 fit A (dotted line) and H1 fit B (dashed line).

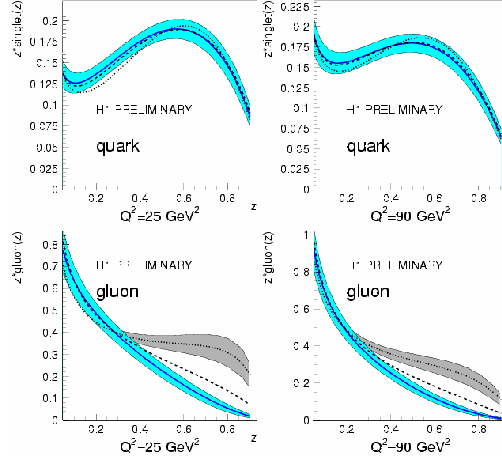


Fig. 40. QCD fits of diffractive singlet- and gluon-distributions using the combined inclusive diffractive and semi-inclusive 2-jet data performed by the H1 collaboration. The combined fit results are compared to the H1 fits A and B from inclusive diffractive data alone.

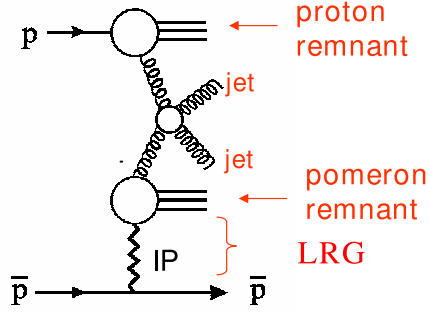


Fig. 41. Schematic diagram of inclusive 2-jet production in $p\text{-}\bar{p}$ collisions.

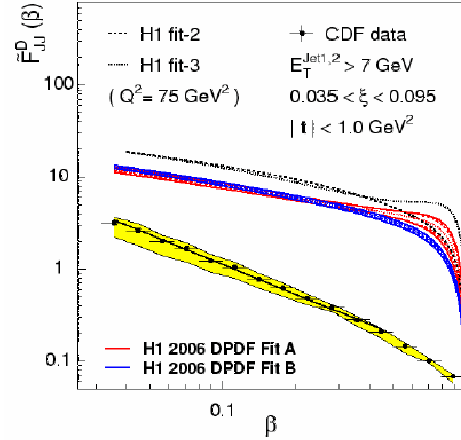


Fig. 42. Diffractive 2-jet production as a function of β measured by CDF at the Tevatron compared to predictions based on H1 fit A and H1 fit B to HERA data.